Applied Surface Science 709 (2025) 163668

Contents lists available at ScienceDirect

Applied Surface Science

journal homepage: www.elsevier.com/locate/apsusc

Full Length Article

Tribocorrosion and antibacterial behaviour of boron-embedded oxide coated Ti45Nb by plasma electrolytic oxidation

Yenal S. Vangolu [a,b,*], Michael G. Bryant [c], Yusuf B. Bozkurt [d], Raghda M. Abdelgawad [e], Reem El-Gendy [e], Richard M. Hall [c], Halim Kovacı [d]

[a] Faculty of Engineering, Department of Metallurgical and Materials Engineering, Atatürk University, Erzurum, Turkiye
[b] Faculty of Engineering, Institute of Functional Surfaces, University of Leeds, Leeds, UK
[c] School of Engineering, Department of Mechanical Engineering, University of Birmingham, Birmingham, UK
[d] Faculty of Engineering, Department of Mechanical Engineering, Atatürk University, Erzurum, Turkiye
[e] Faculty of Medicine and Health, School of Dentistry, University of Leeds, Leeds, UK

ARTICLE INFO

Keywords:
PEO
Tribo-corrosion
Antibacterial
Ti45Nb
Boron
SBF

ABSTRACT

While titanium alloy biomaterials have moderate overall properties, they are often surface-engineered to enhance corrosion resistance, wear, biocompatibility, and antimicrobial qualities. Among various coating processes, PEO is favoured for its ability to embed ions and nanoparticles into the oxide coating. In this study, Ca, P and B-embedded titania layers were successfully formed on the surface of Ti45Nb substrates using PEO. In order to investigate the effect of the boron amount on tribocorrosion and antibacterial/antimicrobial properties, two different boron contents were used in B-embedded coatings. The results were compared with those of the scientific literature. As a result of XRD analyses, anatase and rutile phases, the two main polymorphs of TiO_2, were detected on the substrate surfaces as expected. Ca, P and B ions embedded in the oxide layer were determined by XPS analyses. The simultaneous effects of wear and corrosion in the SBF fluid on the oxide coating with and without B embedment were investigated. At the same time, the impact of the presence of boron ion in the oxide layer and the amount of boron in the electrolyte on antimicrobial/antibacterial properties were analysed.

1. Introduction

The idea of producing biomaterials with properties closest to cortical bone is still one of the most important research topics in the scientific world. Despite all their disadvantages, due to their excellent properties, stainless steel, cobalt alloys, and Ti and Ti alloys are still considered unrivalled, especially in implant production. Nevertheless, among all these biomaterials, Ti and its alloys are the most preferred and used materials in knee and hip joint implants, bone plates, and fracture fixation screws due to their biocompatibility and good corrosion resistance [1–6]. Although Ti6Al4V, an α + β Ti alloy, is currently used commercially in the biomedical field, studies on β-Ti alloys have also increased considerably [7–10]. One of the main reasons for this trend is the mismatch between the elastic modulus of the implant material and the host bone, which can lead to stress shielding, resulting in bone resorption and implant loosening [10–14]. Compared to other biomaterials, their low Young's modulus, often called "bone-like modulus", eases the stress shielding between the bone and the substantially stiffer implant material [15]. Also, their corrosion resistance and biocompatibility have recently brought β-Ti alloys to the forefront.

Among titanium alloys, Ti45Nb is one of the most promising β-Ti alloys, which can be a perfect substitute for cortical bone. Ti45Nb is an appealing material nowadays for biomedical applications because of its good cellular responses and enhanced cellular adhesion and proliferation [16,17]. Some studies showed that Ti45Nb promotes osteoblast activity and inhibits adverse reactions, which is vital for the rapid healing of tissues and reducing the possibility of implant loosening [18–20]. In contrast to their adequate corrosion resistance and good biocompatibility, Ti45Nb alloys have inferior wear and tribocorrosion resistance. For this reason, Ti45Nb alloys, like all other Ti alloys, cannot be used in dynamic contacts such as artificial joint applications inside the human body. The combined effect of wear and corrosion, which defines tribocorrosion, increases material removal at the dynamic contact point. The dissolution of debris in the blood over time and its accumulation in human tissues can lead to health problems such as inflammation, toxicity, carcinogenic response, damage of cell tissue, and

* Corresponding author at: Faculty of Engineering, Department of Metallurgical and Materials Engineering, Atatürk University, Erzurum, Turkiye.
E-mail address: yvangolu@atauni.edu.tr (Y.S. Vangolu).

https://doi.org/10.1016/j.apsusc.2025.163668
Received 24 February 2025; Received in revised form 7 May 2025; Accepted 28 May 2025
Available online 29 May 2025

even loosening of the implant [21].

In the past few decades, surface engineering approaches have been frequently applied to Ti and its alloys to impart desired properties or to enhance their existing ones, such as bioactivity, antibacterial properties, and tribocorrosion behaviour. In this context, there are studies in the scientific literature using many methods, such as PVD, plasma spraying, ion implantation, anodic oxidation, sol–gel coating, plasma electrolytic oxidation (PEO), etc. Among all these methods, PEO stands out as an adjustable technique that enhances surface properties and eases the formation of advanced surface structures through nanoparticle (NP) and/or ion doping [22–27]. While the oxide layer formed by the PEO process provides better resistance to wear and corrosion in the body environment, nanoparticles or ions such as Ga, Au, Cu, Ca, P and B embedded in the structure offer improved osseointegration, bioactivity, biocompatibility and antibacterial properties. Boron-doped oxide coatings have been an intriguing area for researchers in recent years. The incorporation of B in coatings on biomaterial surfaces in specific doses (<20 mg in adults) is biocompatible and has been reported to have many benefits. Boron is a unique trace element that enhances biocompatibility by reducing cytotoxicity and improving cellular adhesion, antibacterial properties, surface hardness, durability, bone integration and healing. Boron also enhances the corrosion resistance of the implant material in the human body [28–32]. In contemporary research, investigations are being conducted regarding the antibacterial properties of boron. Numerous studies have indicated that boron-containing coatings possess direct antibacterial properties against a range of bacterial species, including Staphylococcus aureus, Pseudomonas aeruginosa, and Escherichia coli [33]. Furthermore, additional studies have demonstrated efficacy against biofilm-forming pathogens and multidrug-resistant strains [34]. While the mechanisms underlying this antibacterial effect have not been entirely elucidated, the antibacterial characteristics observed in boron-doped TiO_2 coatings are linked to either the formation of hydroxyl groups or the formation of various compounds consisting of boron and oxygen. [35–38].

Research presented in the scientific literature indicates that calcium phosphate (CaP)- containing coatings produced via the plasma electrolytic oxidation (PEO) method exhibit superior corrosion resistance [39], bioactivity, biocompatibility and antibacterial properties compared to titanium alloy base materials [40,41]. Furthermore, boron doping has been demonstrated to enhance these properties even further [35,36,42–44].

Although numerous publications exist in the literature regarding the investigation on formation of CaP-doped, B-doped, or CaP and B co-doped TiO_2 layers using plasma electrolytic oxidation (PEO), to the best of our knowledge, there currently appears to be no publication in the scientific literature addressing the impact of variations in the amount of boron on both bio-tribocorrosion and antibacterial properties. In this study, using the PEO technique, a boron, Ca and P-embedded titania layer was successfully produced on Ti45Nb alloy. In addition to the desired properties obtained with boron doping, Ca and P were added to make the coating more bioactive and biocompatible. The bio-tribocorrosion and antibacterial properties of the composite coatings formed by varying the amount of boron in the electrolyte content were comparatively investigated.

2. Material and methods

2.1. Sample preparation and coating procedure

Specimens with dimensions of $14 \times 14 \times 3\ mm^3$ were cut from Grade 36 commercial Ti45Nb bars (Nanografi, Turkiye). The samples were ground, polished and ultrasonically cleaned in ethanol and distilled water and dried in air before the process. The coatings were utilised using an AC-pulsed plasma electrolytic oxidation device. The main electrolyte solution consisted of 0.06 M calcium acetate monohydrate ($Ca(C_2H_3O_2)_2{\cdot}H_2O$ – Merck), 0.01 M trisodium phosphate dodecahydrate ($Na_3PO_4{\cdot}12H_2O$ – Merck) and distilled water. In order to vary the amount of boron in the coating structure, three different solutions, E1-E2 and E3, were prepared by adding various amounts of disodium tetraborate decahydrate ($Na_2B_4O_7{\cdot}10H_2O$ – Merck) to the main solution. E1-E2 and E3 solutions contained 0.005 M, 0.01 M and 0.02 M $Na_2B_4O_7{\cdot}10H_2O$, respectively. The process is performed for 5 min at a constant bipolar voltage of + 470/-100 V with a duty cycle of 10 % at 100 Hz. The temperature of the solution was kept constant using a circulation pump, and the electrolyte was stirred continuously at 250 rpm.

2.2. Sample characterisation

The cross-section and surface of the samples were examined and characterised using an energy dispersive spectroscopy (EDS) equipped scanning electron microscope (SEM – ZEISS 300, Germany). SEM and EDS measurements were carried out on the surfaces of the samples before and after the PEO process and after the bio-tribocorrosion tests. The incident beam energy was set to 20 kV for EDS and SEM. The number of pores was calculated from the SEM images using ImageJ software. An X-ray diffractometer (XRD – Panalytical Empyrean, UK) was utilised in continuous scan mode for the phase studies. The source of the device was CuKα ($\lambda = 1.5406$ Å), the generator voltage was 45 kV, the emission current was 40 mA, and the scan rate of the device was 0.0125°/s. X-ray photoelectron spectroscopy (XPS – Specs FlexMod, Germany) measurements were performed to define the chemical states of the elements in oxide films with Monochromatised AlKα X-rays using a Specs Flex-Mod system. The amounts and chemical bondings of Ti, Nb, O, Ca, P and B elements were determined in all samples depending on the peaks obtained via XPS spectra of all samples. The Ar ion etching was applied to the samples to remove surface contaminations and subsequently get better results. The etching processes were carried out till reaching ~ 3 nm depth from the surface at 3 kEV for 10 min in an area of 500x500 μm^2. The etching processes were carried out till reaching ~ 30 nm depth from the surface at 3 kEV for 10 min in an area of 5x5 mm^2. The peak centres of the XPS spectra were determined using Voight fit. In addition, to correct the XPS spectra after etching, the binding energy of the Ar element (243.5 eV) was taken as the reference.

2.3. Bio-tribocorrosion experiments

The combined effect of wear and corrosion on the degradation of coated surfaces was determined using sliding bio-tribocorrosion experiments. A linear reciprocating pin-on-plate tribotester (Turkyus PODWT&RWT, Turkiye), which can simulate bearing surfaces on joint implants, coupled with a potentiostat/galvanostat (Gamry G750, USA), was used for the tests. A standard three-electrode cell was coupled with the device for the in situ electrochemical tests. The pin and plate were immersed in the electrolyte while the specimens were isolated using insulating fixtures.

The tribological tests were performed using an Al_2O_3 ball with a diameter of 6 mm as a counterpart under a normal load of 3 N with a frequency of 1 Hz and a stroke length of 8 mm. For the electrochemical measurements, samples were used as the working electrode (WE), saturated Ag/AgCl electrode was selected as the reference electrode (RE) and graphene electrode was chosen as the counter electrode (CE). All electrochemical experiments were performed in Kokubo's simulated body fluid (SBF) with a temperature of 37 ± 2 °C, the recipe for which can be found in our previous studies. Before sliding, the tribopair's open circuit potential (OCP) was allowed to stabilise for 7200 s. Then, the sliding was activated for 3600 s, and the OCP measurement continued throughout the sliding process. The OCP measurements were performed at 900 s idle before and after wear. The scanning range for potentiodynamic polarisation (PP) experiments was −1; 2.6 V, with a scanning rate of 1 mV/s. As a result of bio-tribocorrosion experiments, wear rates

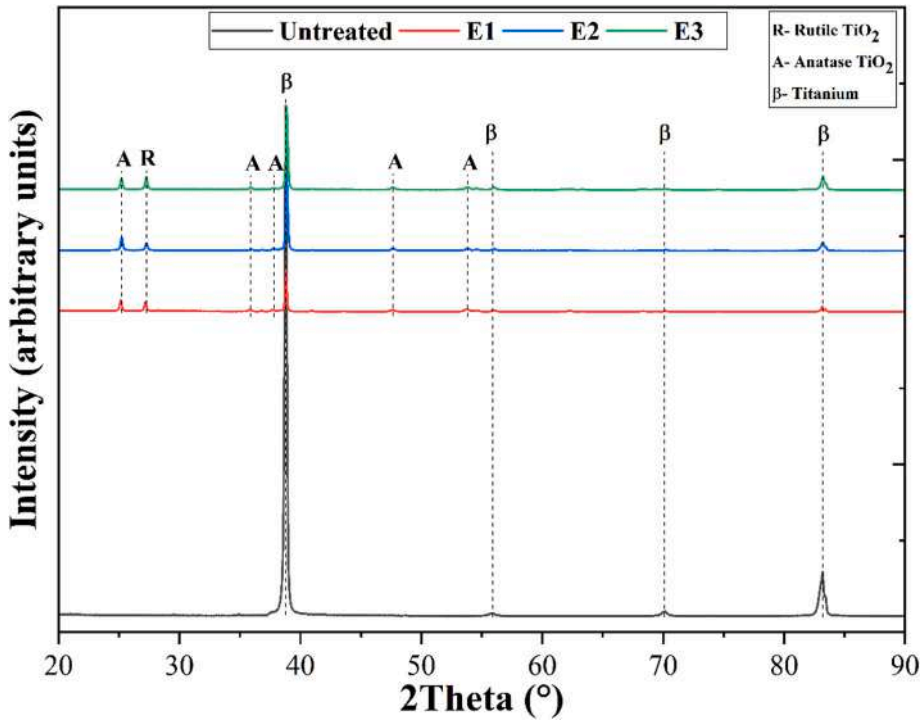

Fig. 1. XRD spectra of untreated and surface-treated samples.

were calculated using the Archard equation $\left(k = \frac{Q}{W}.L\right)$, which depends on mass loss determined by three repeated weighing results. According to the formula, Q represents the missing net volume, W denotes the nominal load, and L signifies the total wear distance.

2.4. Cell viability tests

Leeds Dental and Skeletal Tissue Bank (DREC approval no. 040221/AA/317) supplied the periodontal ligament stem cells (PDLSCs) used in cell viability tests isolated from a donor's first molar. An alpha-modified minimum essential medium, also called alpha MEM complete media, was used to culture the cells. The media was supplemented with 20 % fetal bovine serum (FBS), 2 mM glutamine, and 100 U penicillin/0.1 mg/mL streptomycin. The cells were then incubated at 37 °C, 5 % CO_2. In this work, cells that were 70–80 % subconfluent were employed during passages 4–8, and the medium was changed every 5–7 days. A live/dead viability/cytotoxicity kit designed for mammalian cells (LIVE/DEAD ®, Invitrogen™, Thermo Fisher Scientific, USA) was used to evaluate the viability of PDLSCs in response to various coatings of titanium blocks. ZEN 2012 v. 6.1.7601 software package was utilised to generate the images. Titanium samples were divided into 3 test groups (E1, E2 and E3) according to the coating material applied and one control group. In a 6-well tissue culture plate, triplicate samples of each group were first sterilised under the UV light for 1 hr and then seeded with PDLSCs at a density of $2x10^5$ cells/well. Samples of each group were incubated for 1 week at 37 °C and 5 % CO_2. After incubation, 500 µL of the combined live/dead test reagents were added to each well, and live/dead stain was applied. After that, the plate was then incubated in the dark for 45 min to 1 h at room temperature. A fluorescent microscope (Zeiss, Germany) was used to image the cells after incubation to check the PDLSCs' vitality and how they responded to the coating on the titanium blocks. The cell viability assay experiment was accomplished in 3 biological replicates from one donor. Data were analysed using GraphPad Prism version 10. The one-way ANOVA and Tukey's multiple comparison tests were used to compare the group mean values.

2.5. Antimicrobial tests

According to the boron content of the electrodes used in the coatings, the samples were divided into three test groups, E1, E2 and E3 and uncoated ones were used as a control sample. The specimens were placed in 12-well plates and subjected to sterilisation under UV light for one hour on both sides within the fume hood. *Porphyromonas gingivalis* (*P. gingivalis*) was used in this study to assess the AMR of the applied coat, as it is often linked to subgingival and *peri*-implant infections [45]. Bacteria were cultured from a −80 freezer for 5 days and maintained anaerobically on Fastidious anaerobe agar with 5% horse blood. Bacterial suspensions were prepared using 12 hr culture diluted in fresh Pero-Base broth. OD 600 was adjusted to a concentration of 0.1.

The samples were arranged in a 12-well plate, ensuring the coated surface was oriented upwards. Subsequently, each well containing the test sample was inoculated with 3 ml of *P. gingivalis* (0.1 OD600nm) in Perio-Base broth. The uncoated Ti discs were maintained in a positive culture and a negative media blank. The experiment was done in triplicates, and the samples were incubated for 24 h.

The antibacterial resistance of coated samples was assessed using biofilm formation evaluation and bacterial cell viability calculation, employing live-dead stain and confocal scanning laser microscopy (CSLM). Following the incubation period, the samples underwent a PBS wash and were subsequently stained with the FilmTracer™ LIVE/DEAD® Biofilm viability kit for 30 min under conditions of darkness. A PBS wash was employed to eliminate any surplus stains from the samples. Following this, the samples were placed in a sterile Petri dish with the biofilm facing upwards on the coated surface. Subsequently, they were subjected to observation using a confocal laser scanning microscope. A Leica Microsystems Confocal Laser Scanning Microscope, equipped with a 10× wet lens, was used to obtain the images of the samples. The maximum projection setting was applied to create 3D images. The biofilm image layers were combined to create 2D images using ImageJ software to quantify the biofilm viability (RGB measurement tool) as outlined by [46]. Data were analysed using GraphPad Prism version 10. The one-way ANOVA and Tukey's multiple comparison tests were used to compare the group mean values.

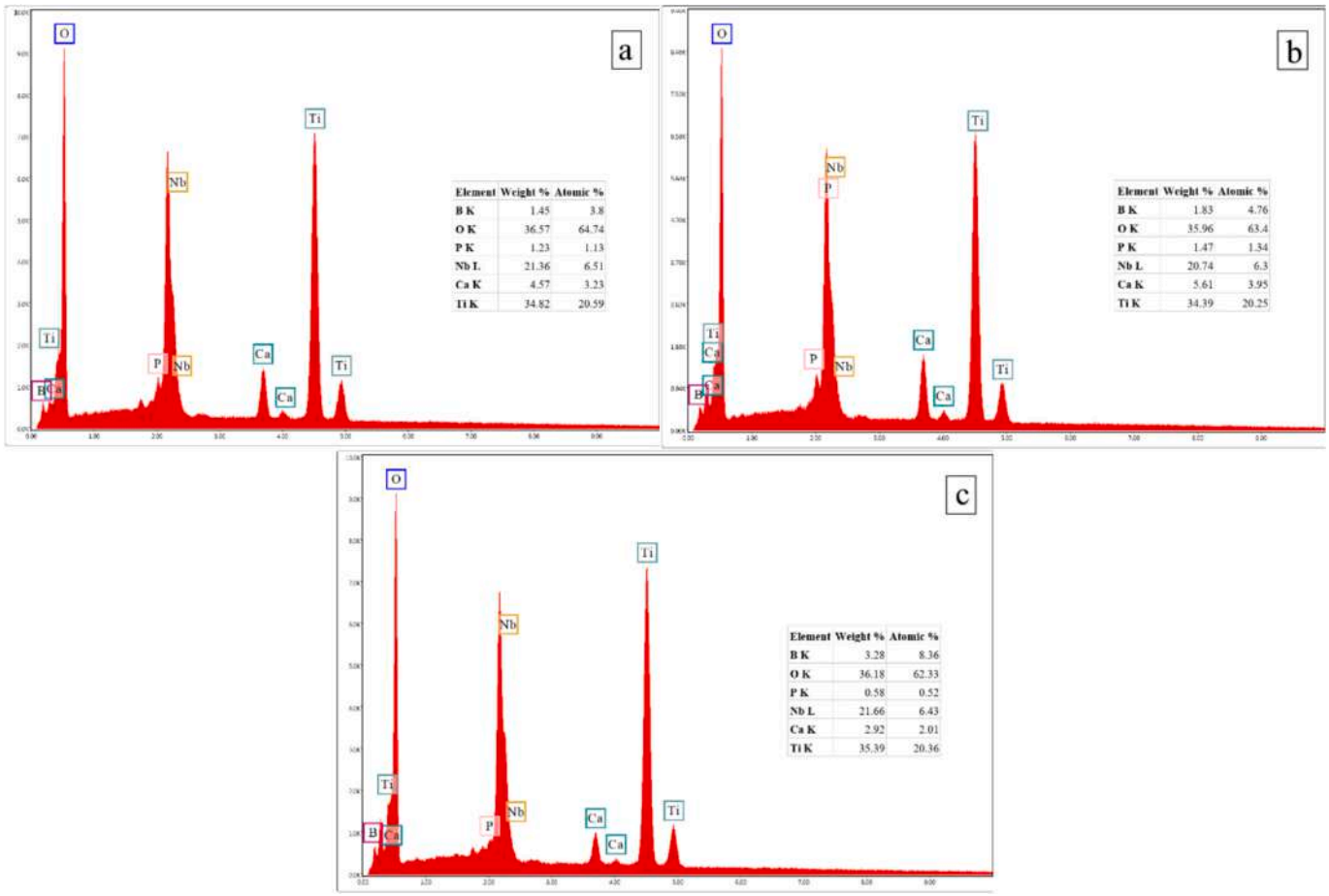

Fig. 2. EDS results of **(a)** E1, **(b)** E2 and **(c)** E3 samples.

3. Results and Discussion

3.1. Structural investigations

The XRD graphs of untreated and PEO-treated Ti45Nb samples are shown in Fig. 1. The XRD patterns of the uncoated samples reveal that only Beta (β)-Ti peaks are reflected from this sample. However, when the PEO-applied samples are examined, it is seen that the intensities of the β-Ti peaks decrease after the treatment in these samples and Anatase (A) and Rutile (R) titanium oxide phases are formed. In addition, the XRD graphs show that the dominant oxide phase for these samples is Anatase (A). Another phenomenon encountered here is that the B structure could not be observed individually or in compound form in the XRD graphs of the B-doped samples. Due to boron's low atomic number, its interaction with X-rays is limited. Even when boron is part of a crystalline phase, its signal can remain weak [47]. The amorphous nature of boron poses additional challenges for XRD analyses. In boron-containing oxides, boron is often in a non-crystalline or amorphous state, which results in a lack of sharp diffraction peaks. Moreover, overlapping peaks may obscure the already weak boron signals. In thin films, diffraction signals are generally low, and given boron's weak scattering characteristics, detecting it via X-ray diffraction (XRD) in thin films is particularly difficult [47,48]. In this context, the absence of boron detection can be attributed to the influence of overlapping peaks, the low atomic number of boron, or the limitations inherent to the thin films.

The EDS analysis results obtained to determine the chemical compositions of Ti45Nb samples coated with oxide using PEO are given in Fig. 2. Here, Ti and Nb peaks were observed in each sample as expected. In addition, although it was not detected in XRD analyses, it was determined in EDS analyses that B was present in the structure of PEO-treated samples. As a result of EDS analyses, the amount of B obtained from E3 was higher than that obtained from E1 and E2. As previously defined in the Material and Methods section, since the amount of B added to the solution was higher in E3 than in E1 and E2, this situation was also confirmed in EDS analyses. In addition, the presence of O in the structure was also proven as a result of EDS analyses, and Ca, P and Cl elements coming from the coating solution were found in the samples.

XPS survey spectrum and high-resolution spectra of PEO treated samples are given in Fig. 3. When the survey spectrum of the samples is examined; it is seen that Ti and Nb peaks belonging to substrate and O, C, Ca and B coming from electrolyte solution are observed. It is seen in both survey and high-resolution spectrum of Ti (Fig. 3a and d), Ti $2p_{3/2}$ and Ti $2p_{1/2}$ peaks are obtained at around 458 eV and 463.7 eV as reported in the literature [49]. Furthermore, the O 1s peak is seen at 530 ev (Fig. 3a), indicating the formation of Ti-O bonds. This result confirms that TiO_2 layers are grown on the substrate. However, when the high-resolution XPS spectra of Ti and O are examined (Fig. 3d and g), it is clearly seen that all the PEO-treated samples show peak shifts. It is mentioned in the literature that the mixed Rutile-Anatase phases in the structure and the film defects can cause peak shifts [50,51]. Therefore, these shifts can be attributed to the mixed phase structure and defects in TiO_2 layers. The survey and high-resolution spectra of Nb are shown in Fig. 3a and e, respectively. The doublet with binding energies of 207.3 eV and 210.05, respectively, has been identified in the literature as belonging to Nb $3d_{5/2}$ and Nb $3d_{3/2}$. These peaks are related to photoelectrons emitted from Nb atoms with a +5 oxidation state (Nb 5+), which indicates the presence of Nb_2O_5 in the structure. In addition, the peaks around 205.65 eV and 208.4 eV are related to Nb $3d_{5/2}$ and Nb $3d_{3/2}$ electrons, which are emitted from Nb atoms with +4 oxidation state (Nb 4+), and this shows the presence of NbO_2 [52]. In light of the

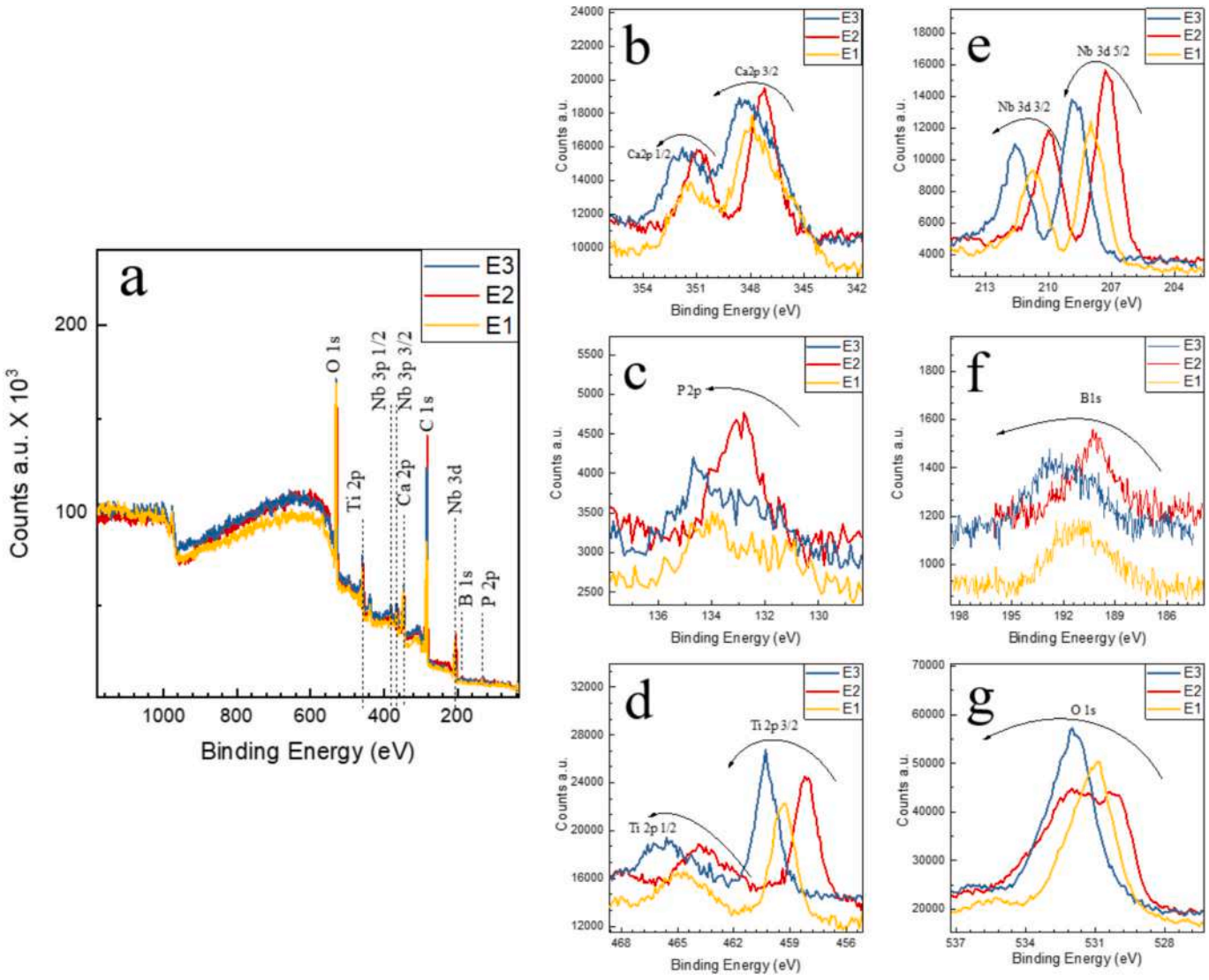

Fig. 3. XPS spectra of surface-treated samples: **(a)** Survey spectrum, high-resolution spectra of **(b)** Ca, **(c)** P, **(d)** Ti, **(e)** Nb, **(f)** B and **(g)** O.

Table 1
The compounds, bond characteristics and ratio of elements obtained from XPS analysis of PEO-treated samples (at.%).

Sample	Elements						Compounds	Bond Character
	Ca ($2p_{3/2}$)	Ti ($2p_{3/2}$)	Nb ($3p_{3/2}$)	O (1s)	P (2p)	B (1s)		
E1	14.80	7.40	3.88	64.64	6.06	3.23	TiO_2 (main)	Ionic + covalent
							Nb_2O_5	Ionic + covalent
E2	8.30	6.46	4.85	68.89	5.77	5.73	NbO_2	Covalent + metallic
							B_2O_3	Covalent
E3	12.06	7.63	3.42	62.42	7.19	7.28	H_3BO_3	Covalent + hydrogen
							TiB_2	Ionic + Covalent + metallic
							BN	Covalent

information given here, in terms of niobium oxide structures formed, it can be seen that the dominant structure for E1 and E3 samples is Nb_2O_5, whereas NbO_2 is dominant for E2 samples. This result highlights the fact that niobium oxide constitutes different forms in the samples. However, no direct relationship exists between the changing electrolyte content and the type of dominant oxide structures formed. The high-resolution spectrum of B is shown in Fig. 3f. The standard binding energy of B 1s in B_2O_3 or H_3BO_3 is 193.0 eV (B-O bond), and in TiB_2 is 187.5 eV (B-Ti bond) [53]. Furthermore, it has been reported that the peak centred at a binding energy of 189.9 eV corresponds to sp^2-BN [54]. In this regard, as can be distinguished from Fig. 3f, while B-O bonds are dominant for E1 and E3, the sp^2-BN bond is dominant for E2. Moreover, the presence of Ca and P in the structures can be seen in Fig. 3b and Fig. 3c. In the literature, the peaks for Ca $2p_{3/2}$ and Ca $2p_{1/2}$ have been reported at the binding energies of around 346.9 eV and 351 eV, respectively [55], consistent with the peak positions in Fig. 3b. In addition to this, P has different valances in its oxides, and the binding energies from 131 eV to 136 eV confirm the presence of phosphorus oxides [56–58]. In this respect, it can be understood from Fig. 3c that PEO-treated samples have various phosphorus oxides. In addition to the information given here,

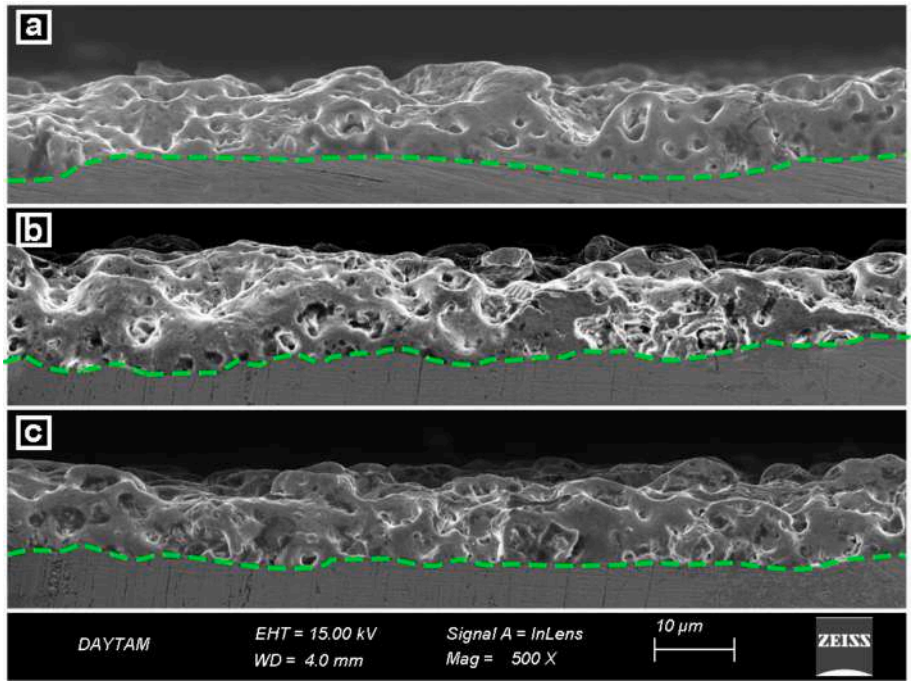

Fig. 4. SEM images showing the cross-section of the samples: **(a)** E1, **(b)** E2 and **(c)** E3.

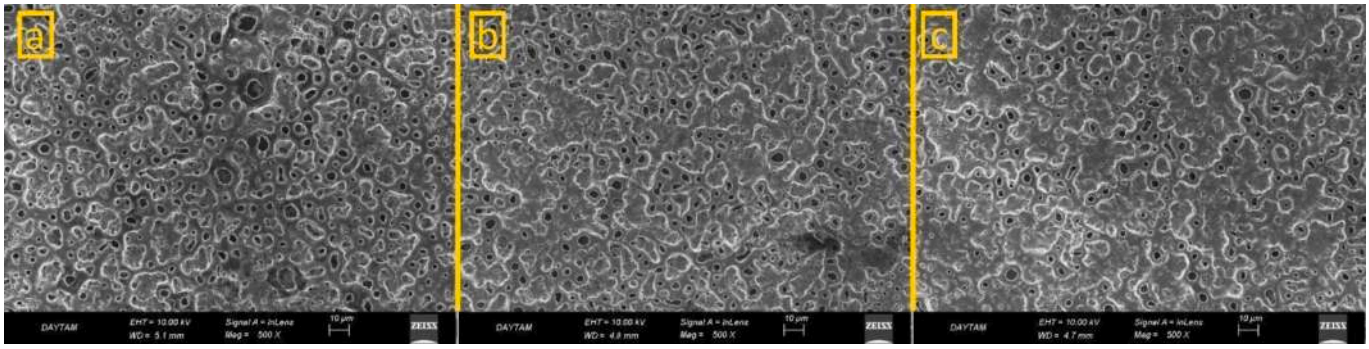

Fig. 5. Surface SEM images of the samples: **(a)** E1, **(b)** E2 and **(c)** E3.

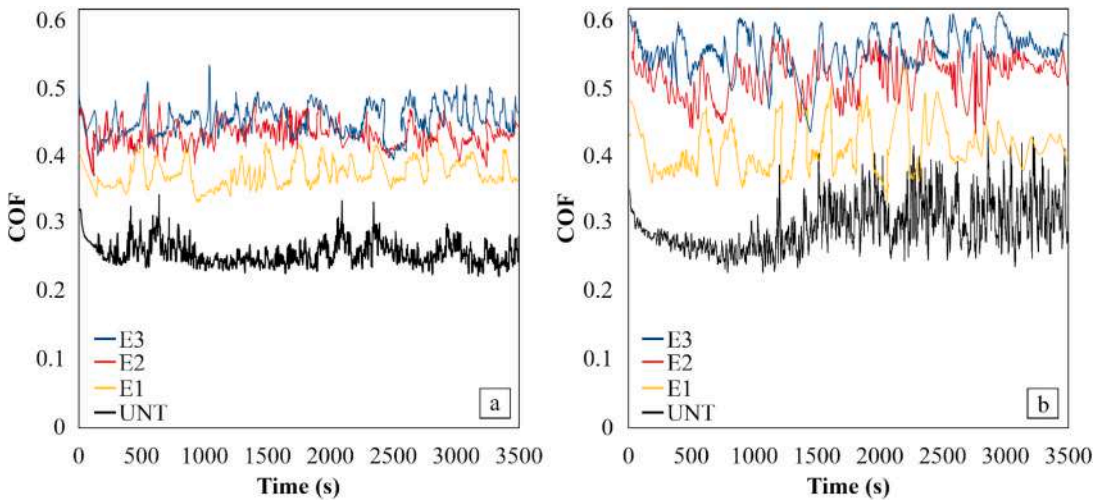

Fig. 6. The coefficients of friction (COFs) for all conditions under **(a)** OCP and **(b)** PP.

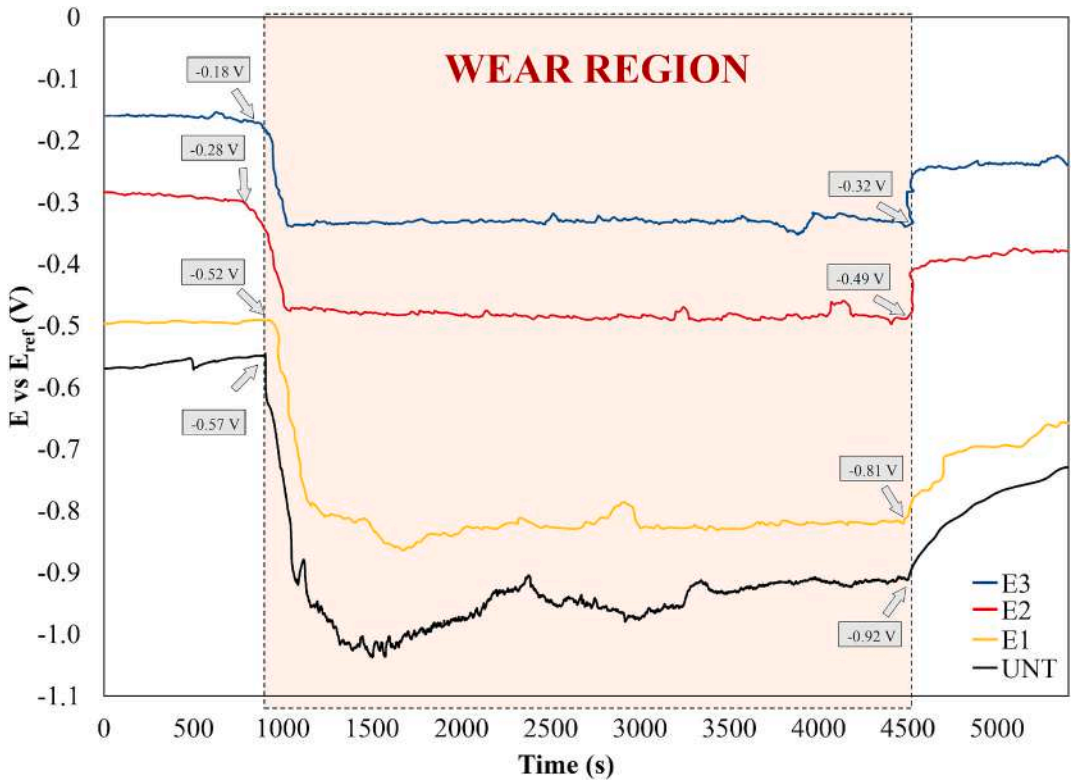

Fig. 7. OCP results for bio-tribocorrosion.

the elemental contents obtained from each PEO-treated sample as a result of XPS analysis are given in Table 1 as atomic percentages. The ratios of Ti and Nb from the substrate and Ca, O, P and B from the solution are given in this table. Here, the ratio of each element varies according to the process conditions, but the most striking point is the ratio of B. The B ratio is E3 > E2 > E1 from high to low, which confirms the B ratios in the solution content given in the material and methods.

The cross-sectional SEM image of the coatings grown using the PEO method is shown in Fig. 4. Here, it is seen that approximately 10 μm of oxide layer has been grown on the Ti45Nb substrate in all samples. This is expected because each sample was subjected to the process under the same coating conditions (current–voltage characteristics and values). In addition, it is understood from this that the changing amount of B element added to the coating solution has not caused any change in the coating thickness. In addition, from the cross-sectional image of each oxide film, it is seen that the films have grown uniformly on the substrates, and there was no separation or lack of adhesion between the substrate and the oxide layers; from this, it is understood that the film-substrate adhesion is relatively high.

Fig. 5 displays the surface SEM pictures of the oxide coatings. It is observed that the oxide films grown on the surface of all samples have a porous structure, as expected, due to the nature of the PEO process. In addition, the quantity of pores following the coating process was recorded as 1092, 652, and 497 for E1, E2, and E3, respectively. It can also be seen that the E2 and E3 samples shown in Fig. 5b and c, respectively, have less porosity than the E1 sample (Fig. 5a). From this point of view, it has been determined that the increasing amount of B-embedding reduces the amount of porosity on the surface, which has also been stated in different literature studies [6,59,60].

3.2. Bio-tribocorrosion investigations

In Fig. 6, the coefficients of friction (COFs) obtained for bio-tribocorrosion experiments performed under OCP (Fig. 6a) and potentiodynamic polarisation (PP) (Fig. 6b) are given. When these graphs are examined, they can explain the changes in the COFs of surface hardness and corrosion products. In both conditions, an increase in the COF is observed on harder surfaces developed with coating. The resistance to abrasive wear increases significantly with the addition of Ca, P and B. In the OCP control, the oscillation in the COF of the untreated sample is lower than that of PP (Fig. 6a). The oscillation in PP starts to show a significant increase after 1000 s. A change in the friction character occurs due to the formation of a brittle oxide layer on the surface in a more intense form of the forced potential. This change is much more marginal in the untreated sample with weaker corrosion resistance (Fig. 6b). The order of COF does not change in the coated samples under PP compared to OCP. However, there are increases in oscillations similar to the untreated surface. This effect shows that harder third-body wear in the bio-tribocorrosion mechanism, especially as the coatings are damaged [61].

Within the scope of bio-tribocorrosion experiments, open circuit potential (OCP) and potentiodynamic polarisation (PP) measurements were taken with reciprocate wear, and the surfaces' performances were analysed. First, the potential values for the measurements taken under OCP were compared (Fig. 7). According to this measurement result, the entry potential of the untreated sample to the wear zone is −0.57 V, the lowest value. The exit potential is −0.91 V. It also represents the weakest corrosion resistance among the exit potentials. In contrast to the untreated sample, a positive increase is observed in E1. The more noble surface character shows the existence of wear under the natural potential. In this context, the entry potential increases by 0.05 V. This difference in the exit potential increases to 0.11 V. Thus, the contribution of Ca, P and B elements to bio-tribocorrosion is minimal in this condition. Under E2 and E3 conditions, the potentials climb more significantly, especially with the increase in P and B contribution. In the E2 condition, the entry potential increases by approximately 50%, reaching −0.28 V. Similarly, the output potential is also quite high (−0.49 V). The noblest behaviour is obtained from the E3 surface. The input potential is about three times higher than the untreated surface. The output potential reaches −0.32 V. In the wear zone, the potential swing is higher in the untreated sample. The swing is lower on more noble and harder

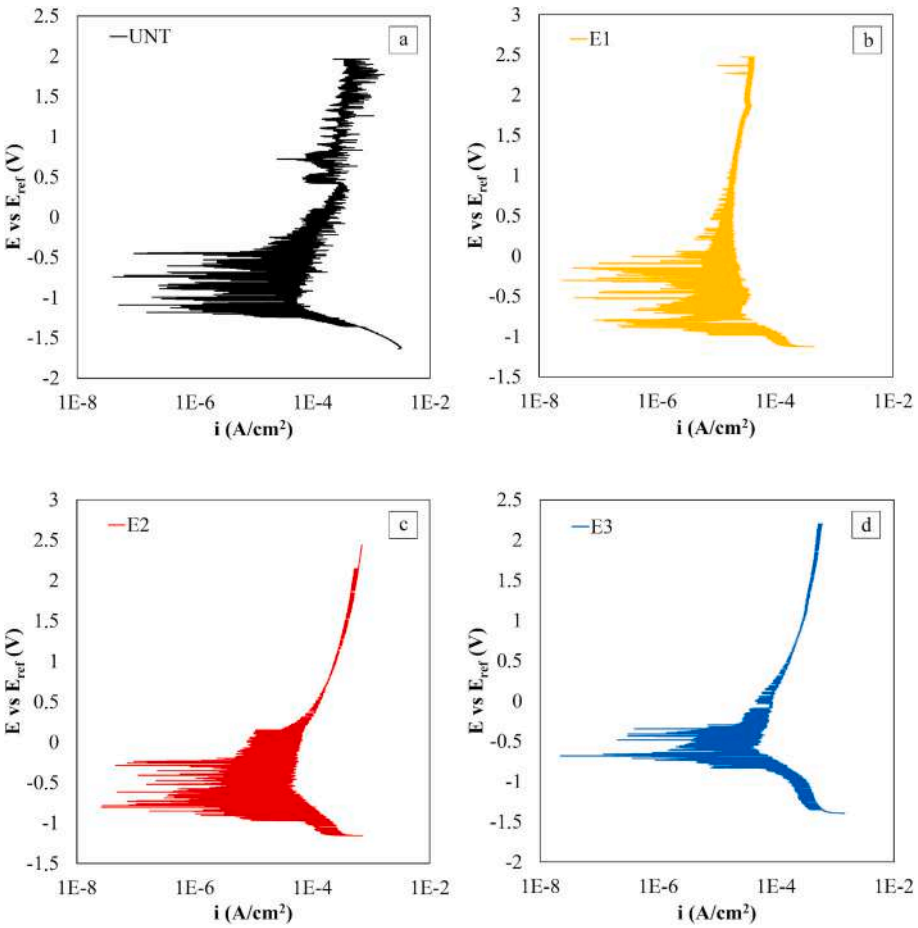

Fig. 8. The potentiodynamic polarisation test results of the samples conducted from the wear tests: **(a)** untreated, **(b)** E1, **(c)** E2 and **(d)** E3.

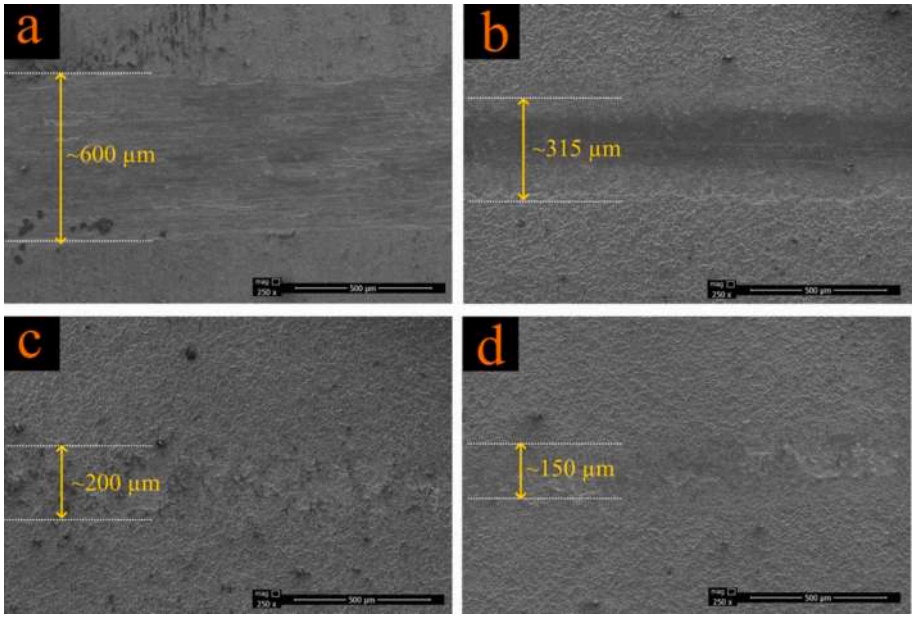

Fig. 9. The surface SEM images of the samples after the tests performed under open circuit potential: **(a)** untreated, **(b)** E1, **(c)** E2 and **(d)** E3.

surfaces.

In Fig. 8, curves belonging to samples polarised under reciprocating are given for all samples. Unlike the curves under OCP, the bio-tribocorrosion effect has become much more damaging in samples exposed to intense corrosion attacks. The impact of the complex mechanism on the surfaces can be defined by the unstable current density, especially in the anodic branches of the curves [62]. This situation continues even for the Tafel region and beyond for the untreated sample

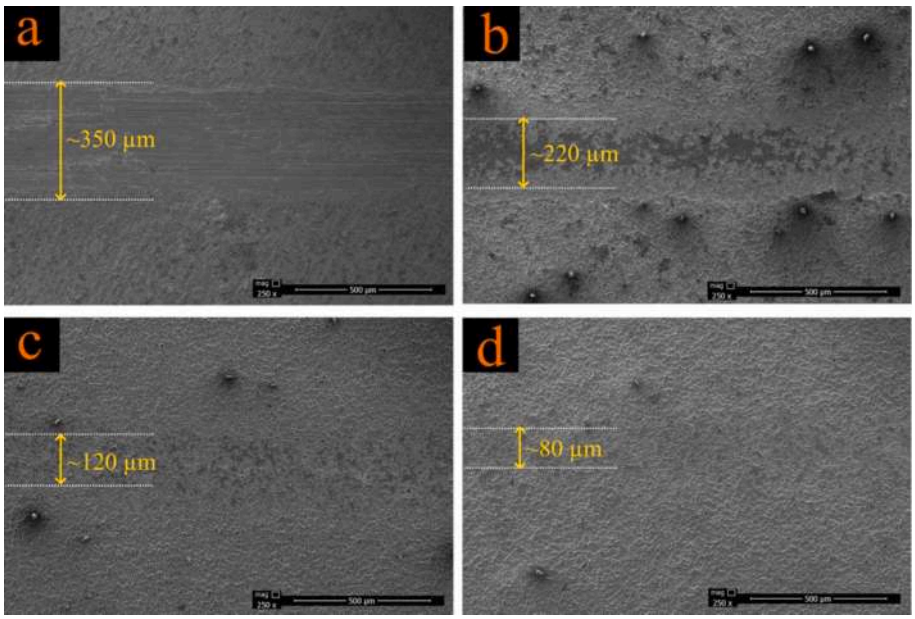

Fig. 10. The surface SEM images of the samples after the tests performed under potentiodynamic polarisation: **(a)** untreated, **(b)** E1, **(c)** E2 and **(d)** E3.

(Fig. 8a). For coated samples, the oscillation in the region where oxygen reduction starts and ends has decreased considerably. Thus, the corrosion rate amounts have decreased for surfaces that exhibit relatively inert behaviour against stronger oxygen attacks [63]. As a result, the material loss due to corrosion within the tribocorrosion mechanism has decreased (Fig. 8b–d). Therefore, the coating morphology has contributed not only to the wear performance but also to the corrosion performance. However, this change is not as substantial as the wear performance. Nevertheless, it is possible to state that the corrosion potentials in the coated samples have increased positively.

Fig. 9 shows the surfaces of the samples after the tests performed under OCP. When the figure is examined, it is determined that the widest wear scar width is observed in the untreated sample, while the scar width in the coated samples is narrower compared to the untreated sample. Moreover, the scar width decreases further with the increase in the B additive ratio. The lowest scar width among the coated samples is observed in the E3 sample with the highest B additive ratio. Fig. 10 shows the surfaces after the tests performed under potentiodynamic polarisation. When this figure is examined, similar to the results obtained in the open circuit potential tests, the untreated sample has the highest wear scar width. In contrast, the trace width of the coated samples is lower than that of the untreated sample, and the narrowest wear scar width is observed in the E3 sample with the highest B content. When Fig. 9 and Fig. 10 are examined comparatively, it is seen that the wear track width observed under potentiodynamic polarisation conditions in all samples, whether untreated or coated, is lower than the track widths under open circuit potential conditions. This result is a condition because, contrary to the potentiodynamic polarisation condition, there is no forced potential in the tests performed at open circuit potential. The first thing that stands out for both experimental conditions is that the amount of wear on the coated samples is lower than the uncoated samples. This is an expected situation. Because the oxide films grown on the Ti45Nb material increase the resistance to wear load due to their high hardness, these films prevent wear by showing lubricating properties. However, the remarkable point for both test conditions is that the amount of wear decreases with increasing B content in the coated samples. This is thought to be due to the increase in TiO_2 film hardness with increasing B content. It has been stated in the literature that the hardness of TiO_2 increases when B is added to the structure [64], and it is understood from this that the increasing amount of B addition provides a further increase in hardness values. Therefore, the best plastic deformation and consequent tribocorrosion resistance are obtained from the sample with the highest B content for both open circuit potential and potentiodynamic polarisation conditions.

Beyond these conclusions, another critical issue is the wear mechanism seen in the samples. It is observed that the untreated samples are subjected to severe adhesive wear under both OCP and PP conditions. In both situations, material accumulations at the edges of the wear marks are observed because of the plastic deformation caused by the applied load in untreated samples (Fig. 9a and Fig. 10a). However, it is noted that the coated samples exhibit less of this plastic deformation effect. Despite adhesive wear being seen in the PEO-treated samples at E1 conditions, partial micro scratches are observed when the wear marks are examined. This indicates that in addition to adhesive wear, these samples are subjected to abrasive wear because of the effect of the detached oxide particles coming from the surface and salt particles coming from the solution (Fig. 9b and Fig. 10b). Moreover, it is understood from the relevant images that the E2 sample is exposed to less wear compared to the untreated samples as expected. The oxide layer on the surface of this sample increases the resistance to plastic deformation due to its high hardness, provides support to the substrate in terms of bearing the wear load and has a wear-reducing effect due to the lubricating effect of the film.

Another noteworthy point is that wear occurs at much lower levels in E2 and E3 samples compared to other samples. While abrasive wear, albeit relatively superficial, is observed in E2 samples (Fig. 9c and Fig. 10c), wear marks are almost invisible in E3 samples (Fig. 9d and Fig. 10d). From this, it is understood that the increasing amount of B additive has an effect on increasing the tribocorrosion resistance, which can be attributed to the increase in TiO_2 film hardness with the increase in B amount, as mentioned before. For this reason, the highest tribocorrosion resistance among the coated samples is observed in the E3 sample, which has the highest B additive. The results show that the hard oxide layer formed on the surface by the PEO process improves the tribocorrosion resistance of Ti45Nb, which increases with the increase in the B ratio.

It was observed that the wear rates obtained by conducting wear tests with OCP were higher under more dominant wear damage and for the same samples compared to PP. There is a similar order in wear rates proportional to the trace widths for OCP. According to this calculation, the wear rate in the untreated sample is on average 5.95×10^{-4} mm^3/Nm. The wear rates for E1, E2 and E3 conditions are 1.16×10^{-4} mm^3/

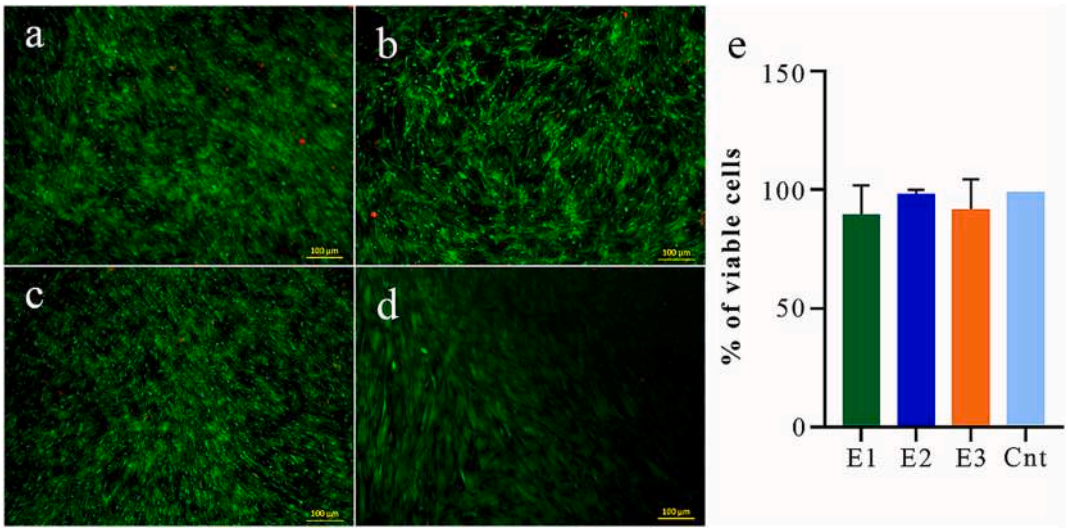

Fig. 11. The effect of the amount of boron for **(a)** E1, **(b)** E2, **(c)** E3, and **(d)** control samples on the viability of PDLCs after 7 days of incubation. **(e)** the percentage of live cells.

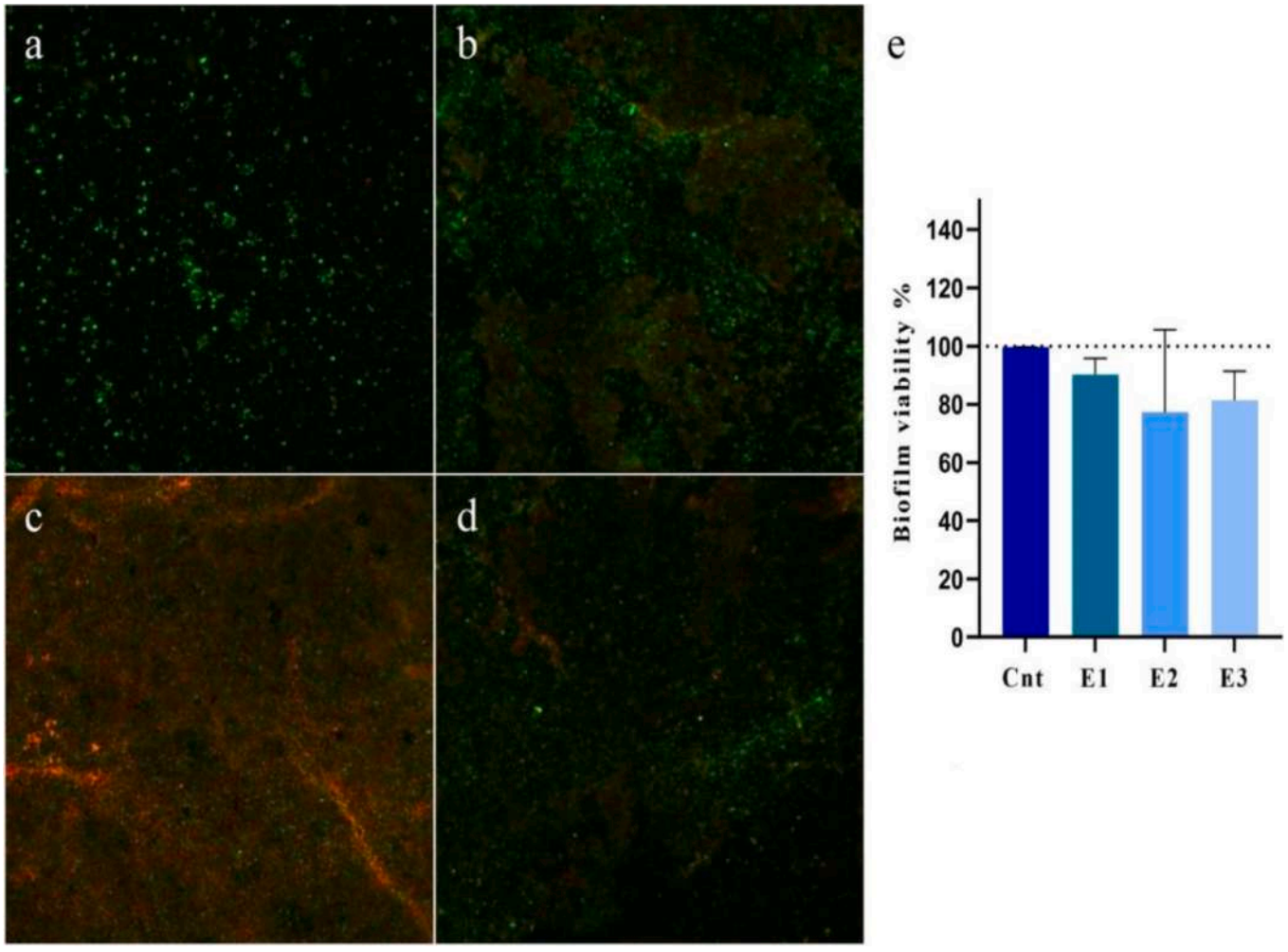

Fig. 12. CLSM Images of *P.gingivalis* biofilms after 24 h of growth on coated Ti blocks. Confocal images of a) Control, b) E1, c) E2 and d) E3 samples in 2D maximum projection, combining all 3D layers and e) Live/Dead ratio calculated by the area of red and green within the maximum projection images.

Nm, 9.88 × 10^{-5} mm^3/Nm and 8.75 × 10^{-5} mm^3/Nm, respectively. When the experiments were calculated for PP controlled wear tests, it was determined that the order between the specimens did not change. In this context, the wear rate for PP in the untreated sample decreased to 1.22 × 10^{-4} mm^3/Nm compared to OCP. This decreasing trend also includes the coated samples. The wear rate for E1 is 8.43 × 10^{-5} mm^3/Nm,

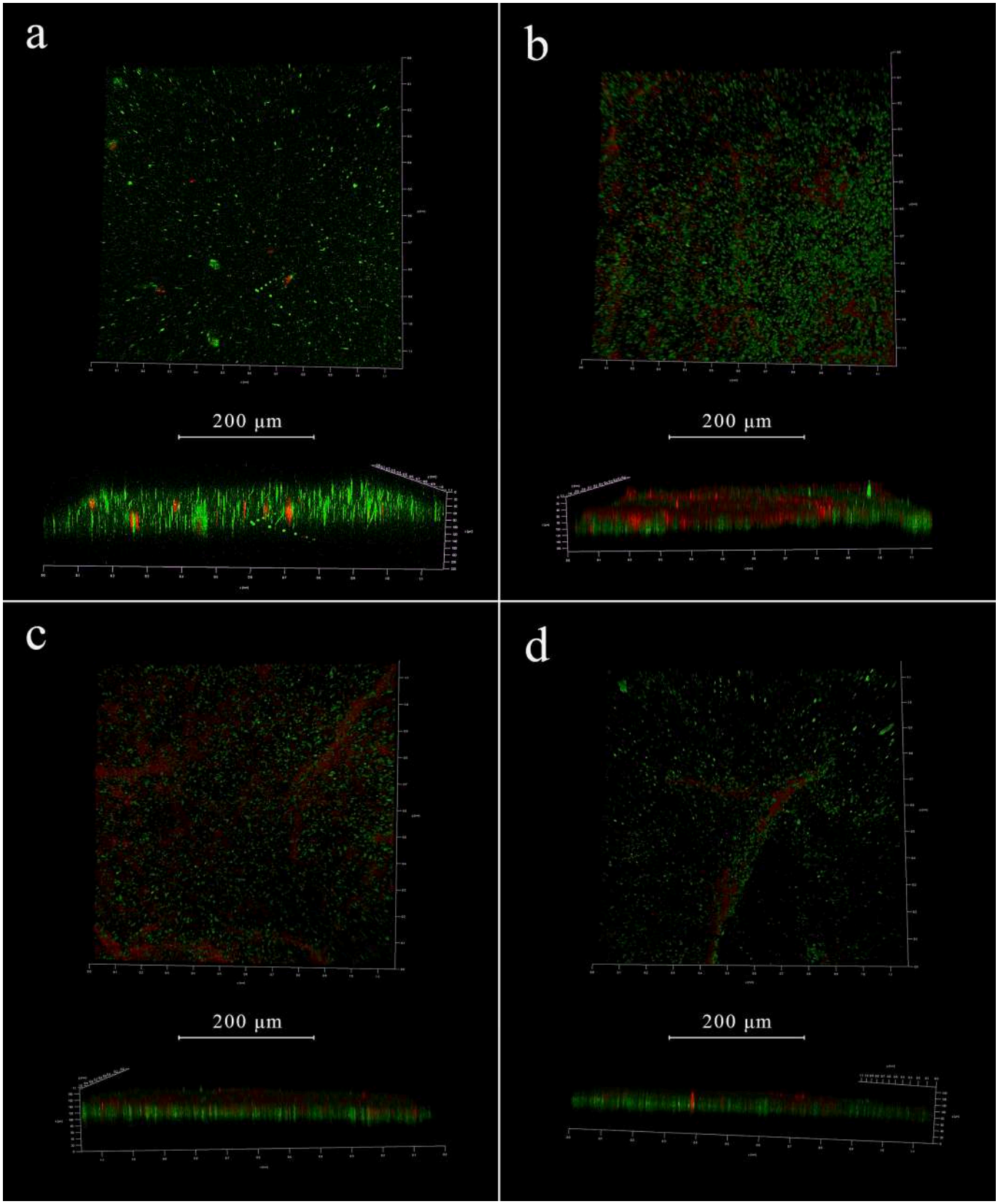

Fig. 13. 3D *P.gingivalis* biofilm images of a) Control, b)E1, c) E2 and d) E3 samples in two different plans.

for E2 3.66 × 10^{-5} mm^3/Nm, and finally for E3 it is 2.12 × 10^{-5} mm^3/Nm. Based on all these measurements, it can be concluded that the trace widths increase in direct proportion to the trace depths based on mass loss.

3.3. Cell viability investigations

Fluorescent microscopic images were taken after 7 days of incubation of PDLCs with the titanium blocks coated with the three test materials (E1, E2, and E3) (Fig. 11a-d). Most of the cells are viable (stained green) with minimal cell death (cells stained red) and acquire a spindle morphology, indicating cell attachment to the surfaces. All test samples are comparable to the control. The percentage of viable cells was calculated by Image J analysis using this equation:

Viability (%) = [(*ratio of viable cells* (*green*)/*total of live and d ead cells*)] × 100. The mean percentage of cell viabilities was calculated as 99.52 ± 0.53, 97.97 ± 1.55, 95.19 ± 2.42, and 96.11 ± 1.00 for control, E1, E2, and E3, respectively. As illustrated by the results and in Fig. 11e, no significant differences were observed between the three tests and the control samples ($p = 0.4857$).

3.4. Antimicrobial investigations

The results show that the 24-hour *P. gingivalis* biofilm is grown on the samples of each group (Fig. 12a-d and Fig. 13a-d). A different percentage of viability is shown depending on the boron amount of the applied coating. E2 samples show the lowest percentage of biofilm viability compared to E1, E3 and the control uncoated group. E3 samples show the least biofilm density compared to the other two experimental groups (Fig. 12e). Mean percentage of biofilm viabilities was calculated as 99.17 ± 0.31, 90.27 ± 5.49, 77.21 ± 28.31, and 81.31 ± 10.06 for control, E1, E2, and E3, respectively ($p = 0.361$). The results show that there was no statistically significant difference found between the boron-doped groups.

4. Conclusions

In this study, boron and Ca-P doped titania layers with a thickness of app. 10 μm were successfully formed on the surfaces of Ti45Nb specimens by the PEO method. XRD analyses revealed the formation of anatase and rutile phases of TiO_2 on the substrate surfaces. Although not observed in XRD graphs, EDS and XPS analysis confirmed the presence of Ca, P and B in the film layer. According to SEM images, the oxide layer had a rough and porous structure, which is of great importance for osseointegration and bone growth. The porosity was relatively low in the samples with higher boron content. The addition of boron increased the tribocorrosion resistance of all coated materials. These properties were found to be directly proportional to the increasing amount of boron in the electrolyte. It was determined that E3 samples with the highest boron content showed relatively the best resistance to the combined effect of wear and corrosion. The coatings were not found to significantly affect the viability of periodontal ligament stem cells (PDLSCs), indicating that B-doping in given amounts did not negatively affect the biocompatibility of Ti45Nb. All boron-doped coatings exhibited antimicrobial properties against *P. gingivalis* compared to control samples. Although sample E2 showed the lowest biofilm viability percentage, considering the margins of error, it can be said that E2 and E3 actually have similar antibacterial properties. This can be explained by the fact that the antibacterial properties of the surface are relatively better at higher boron amounts.

In general, the results of this study suggest that boron-doped titania coatings on Ti45Nb by PEO can enhance both bio-tribocorrosion resistance and antimicrobial properties while maintaining biocompatibility, making them promising for biomedical applications.

CRediT authorship contribution statement

Yenal S. Vangolu: Writing – review & editing, Writing – original draft, Visualization, Validation, Supervision, Methodology, Investigation, Funding acquisition, Conceptualization. **Michael G. Bryant:** Writing – review & editing, Validation, Supervision, Resources, Project administration, Conceptualization. **Yusuf B. Bozkurt:** Writing – original draft, Visualization, Investigation, Formal analysis. **Raghda M. Abdelgawad:** Validation, Investigation, Formal analysis. **Reem El-Gendy:** Writing – original draft, Validation, Supervision, Methodology, Investigation, Formal analysis. **Richard M. Hall:** Supervision, Resources, Methodology, Funding acquisition. **Halim Kovacı:** Writing – review & editing, Writing – original draft, Validation, Supervision, Methodology, Investigation, Formal analysis.

Declaration of competing interest

The authors declare the following financial interests/personal relationships which may be considered as potential competing interests: Yenal S. Vangolu reports a relationship with The Scientific and Technological Research Council of Türkiye (TUBITAK) that includes: funding grants and travel reimbursement. If there are other authors, they declare that they have no known competing financial interests or personal relationships that could have appeared to influence the work reported in this paper.

Acknowledgement

Dr Yenal S. Vangölü would like to thank the TUBITAK (The Scientific and Technological Research Council of Turkiye)-BIDEB 2219 postdoctoral research fellowship programme, which supported this study and enabled him to be an academic visitor at the University of Leeds, UK. The authors would like to thank Atatürk University East Anatolia High Technology Application and Research Center (DAYTAM) and Erzurum Technical University High Technology Application and Research Center (YUTAM) for their assistance in characterising samples.

Data availability

Data will be made available on request.

References

[1] J. Quinn, R. McFadden, C.W. Chan, L. Carson, Titanium for orthopedic applications: an overview of surface modification to improve biocompatibility and prevent bacterial biofilm formation, Iscience 23 (2020) 101745, https://doi.org/10.1016/J.ISCI.2020.101745.
[2] W. Abd-Elaziem, M.A. Darwish, A. Hamada, W.M. Daoush, Titanium-based alloys and composites for orthopedic implants Applications: A comprehensive review, Mater. Des. 241 (2024) 112850, https://doi.org/10.1016/J.MATDES.2024.112850.
[3] A.K. Gain, L. Zhang, S. Lim, Tribological behavior of Ti–6Al–4V alloy: Subsurface structure, damage mechanism and mechanical properties, Wear 464–465 (2021) 203551, https://doi.org/10.1016/J.WEAR.2020.203551.
[4] P. Siahpour, S.M.T. Omar, D. Griffin, M.Y. Amegadzie, A. Tieu, I.W. Donaldson, K. P. Plucknett, Evaluating surface mechanical properties and wear resistance of Ti–6Al–4V alloy subjected to ultrasonic pulsed waterjet peening, Wear 550–551 (2024) 205400, https://doi.org/10.1016/J.WEAR.2024.205400.
[5] M.E. Hoque, N.N. Showva, M. Ahmed, A. Bin Rashid, S.E. Sadique, T. El-Bialy, H. Xu, RETRACTED: Titanium and titanium alloys in dentistry: Current trends, recent developments, and future prospects, Heliyon 8 (2022) e11300, https://doi.org/10.1016/J.HELIYON.2022.E11300.
[6] P. Molaeipour, S.R. Allahkaram, S. Akbarzadeh, Corrosion inhibition of Ti6Al4V alloy by a protective plasma electrolytic oxidation coating modified with boron carbide nanoparticles, Surf. Coat. Technol. 430 (2022) 127987, https://doi.org/10.1016/J.SURFCOAT.2021.127987.
[7] G. Senopati, R.A. Rahman Rashid, I. Kartika, S. Palanisamy, Recent development of low-cost β-ti alloys for biomedical applications: A Review, Metals 13 (2023) 194, https://doi.org/10.3390/MET13020194.
[8] N.L. Church, A. Prasad, N.G. Jones, On the design of low modulus Ti–Nb–Au alloys for biomedical applications, J. Mech. Beha.v Biomed. Mater. 157 (2024) 106633, https://doi.org/10.1016/J.JMBBM.2024.106633.

[9] E. Alabort, Y.T. Tang, D. Barba, R.C. Reed, Alloys-by-design: A low-modulus titanium alloy for additively manufactured biomedical implants, Acta. Mater. 229 (2022) 117749, https://doi.org/10.1016/J.ACTAMAT.2022.117749.
[10] G. Yamako, E. Chosa, K. Totoribe, S. Hanada, N. Masahashi, N. Yamada, E. Itoi, In-vitro biomechanical evaluation of stress shielding and initial stability of a low-modulus hip stem made of β type Ti-33.6Nb-4Sn alloy, Med. Eng. Phys. 36 (2014) 1665–1671, https://doi.org/10.1016/J.MEDENGPHY.2014.09.002.
[11] M.M. Shahzamanian, R. Banerjee, N.B. Dahotre, A.R. Srinivasa, J.N. Reddy, Analysis of stress shielding reduction in bone fracture fixation implant using functionally graded materials, Compos. Struct. 321 (2023) 117262, https://doi.org/10.1016/J.COMPSTRUCT.2023.117262.
[12] M. Qiang, X. rong Yang, X. yan Liu, G. jie Wang, J. zhong Wang, Enhanced yield stress and reduced elastic modulus of metastable β Ti–Nb alloys deformed by equal channel angular pressing attributed to the Synergistic effect of deformation mechanisms, Mater. Sci. Eng.: A 909 (2024) 146858, https://doi.org/10.1016/J.MSEA.2024.146858.
[13] T. Jia, D. Guines, D.M. Gordin, L. Leotoing, T. Gloriant, Finite element analysis of a low modulus Ti-20Zr-3Mo-3Sn alloy designed to reduce the stress shielding effect of a hip prosthesis, J. Mech. Behav. Biomed. Mater. 157 (2024) 106640, https://doi.org/10.1016/J.JMBBM.2024.106640.
[14] R.M. Namus, W.M. Rainforth, Investigating the relevance of TiNbTaZr high entropy alloy for orthopaedic applications, Wear 548–549 (2024) 205393, https://doi.org/10.1016/J.WEAR.2024.205393.
[15] A.X.Y. Guo, B. Cao, Z. Wang, X. Ma, S.C. Cao, Fabricated high-strength, low-elastic modulus biomedical Ti-24Nb-4Zr-8Sn alloy via powder metallurgy, Materials 16 (2023) 3845, https://doi.org/10.3390/MA16103845.
[16] J. Tan, J. Li, Z. Ran, J. Wu, D. Luo, B. Cao, L. Deng, X. Li, W. Jiang, K. Xie, L. Wang, Y. Hao, Accelerated fracture healing by osteogenic Ti45Nb implants through the PI3K–Akt signaling pathway, Biodes. Manuf. 6 (2023) 718–734, https://doi.org/10.1007/S42242-023-00250-6/FIGURES/8.
[17] Y. Chen, P. Han, A. Dehghan-Manshadi, D. Kent, S. Ehtemam-Haghighi, C. Jowers, M. Bermingham, T. Li, J. Cooper-White, M.S. Dargusch, Sintering and biocompatibility of blended elemental Ti-xNb alloys, J. Mech. Behav. Biomed. Mater. 104 (2020) 103691, https://doi.org/10.1016/J.JMBBM.2020.103691.
[18] C.E. Tanase, M. Golozar, S.M. Best, R.A. Brooks, Cell response to plasma electrolytic oxidation surface-modified low-modulus β-type titanium alloys, Colloids. Surf. B Biointerfaces 176 (2019) 176–184, https://doi.org/10.1016/J.COLSURFB.2018.12.064.
[19] I. Lauria, T.N. Kutz, F. Böke, S. Rütten, D. Zander, H. Fischer, Influence of nanoporous titanium niobium alloy surfaces produced via hydrogen peroxide oxidative etching on the osteogenic differentiation of human mesenchymal stromal cells, Mater. Sci. Eng. C 98 (2019) 635–648, https://doi.org/10.1016/J.MSEC.2019.01.023.
[20] I. Jirka, M. Vandrovcová, O. Frank, Z. Tolde, J. Plšek, T. Luxbacher, L. Bačáková, V. Starý, On the role of Nb-related sites of an oxidized β-TiNb alloy surface in its interaction with osteoblast-like MG-63 cells, Mater. Sci. Eng. C 33 (2013) 1636–1645, https://doi.org/10.1016/J.MSEC.2012.12.073.
[21] J. Ureña, S. Tsipas, A.M. Pinto, F. Toptan, E. Gordo, A. Jiménez-Morales, Corrosion and tribocorrosion behaviour of β-type Ti-Nb and Ti-Mo surfaces designed by diffusion treatments for biomedical applications, Corros. Sci 140 (2018) 51–60, https://doi.org/10.1016/J.CORSCI.2018.06.024.
[22] H. Arab, G.L. Chiarello, E. Selli, G. Bomboi, A. Calloni, G. Bussetti, G. Albani, M. Bestetti, S. Franz, Ni-Doped Titanium Dioxide Films Obtained by Plasma Electrolytic Oxidation in Refrigerated Electrolytes, Surfaces 3 (2020) 168–181, https://doi.org/10.3390/SURFACES3020013.
[23] J. Meng, S. Wang, Q. Guan, X. Dong, L. Li, H. Yu, H. Li, Fabrication and performance of composite coating doped with CeO2 nanoparticles by plasma electrolytic oxidation on Cu–Zn alloy surface, J. Appl. Electrochem. 53 (2023) 2347–2357, https://doi.org/10.1007/S10800-023-01926-8/FIGURES/8.
[24] W. Lv, X. Lu, Q. Chen, J. Ma, S.A. Karpushenkov, O.V. Ignatenko, F. Wang, Influence of Cr Nanoparticles on Plasma Electrolytic Oxidation Coatings on AM50 Mg Alloy, Coatings 13 (2023) 1196, https://doi.org/10.3390/COATINGS13071196.
[25] C. Yang, S. Cui, Z. Wu, J. Zhu, J. Huang, Z. Ma, R.K.Y. Fu, X. Tian, P.K. Chu, Z. Wu, High efficient co-doping in plasma electrolytic oxidation to obtain long-term self-lubrication on Ti6Al4V, Tribol. Int 160 (2021) 107018, https://doi.org/10.1016/J.TRIBOINT.2021.107018.
[26] S.S. Nisar, H.C. Choe, TiO2 coatings doped with MoS2 nanoparticles using plasma electrolytic oxidation on Ti–6Al–4V alloy: Application for enhanced and functional bio-implant surface, J. Mater. Res. Technol. 33 (2024) 2035–2056, https://doi.org/10.1016/J.JMRT.2024.09.185.
[27] K.V. Nadaraia, S.N. Suchkov, N.S. Markin, I.M. Imshinetskiy, S.I. Ivannikov, D. V. Mashtalyar, A.Y. Ustinov, S.L. Sinebryukhov, S.V. Gnedenkov, Electrochemical synthesis of boron-containing coatings on Mg alloy for thermal neutron shielding, J. Magnesium Alloys 11 (2023) 3779–3789, https://doi.org/10.1016/J.JMA.2023.09.018.
[28] A.E. Pazarçeviren, A. Tezcaner, D. Keskin, S.T. Kolukısa, S. Sürdem, Z. Evis, Boron-doped Biphasic Hydroxyapatite/β-Tricalcium Phosphate for Bone Tissue Engineering, Biol. Trace. Elem. Res. 199 (2021) 968–980, https://doi.org/10.1007/S12011-020-02230-8/FIGURES/6.
[29] X. Ying, S. Cheng, W. Wang, Z. Lin, Q. Chen, W. Zhang, D. Kou, Y. Shen, X. Cheng, F.A. Rompis, L. Peng, C.Z. Lu, Effect of boron on osteogenic differentiation of human bone marrow stromal cells, Biol. Trace. Elem. Res. 144 (2011) 306–315, https://doi.org/10.1007/S12011-011-9094-X/FIGURES/4.
[30] H. Khaliq, Z. Juming, P. Ke-Mei, The Physiological Role of Boron on Health, Biol. Trace. Elem. Res. 186 (2018) 31–51, https://doi.org/10.1007/S12011-018-1284-3/TABLES/4.
[31] L. Sopchenski, S. Cogo, M.F. Dias-Ntipanyj, S. Elifio-Espósito, K.C. Popat, P. Soares, Bioactive and antibacterial boron doped TiO2 coating obtained by PEO, Appl Surf Sci 458 (2018) 49–58, https://doi.org/10.1016/J.APSUSC.2018.07.049.
[32] S.S. Hakki, B.S. Bozkurt, E.E. Hakki, Boron regulates mineralized tissue-associated proteins in osteoblasts (MC3T3-E1), J. Trace Elem. Med Biol. 24 (2010) 243–250, https://doi.org/10.1016/J.JTEMB.2010.03.003.
[33] D. Celebi, A. Taghizadehghalehjoughi, S. Baser, S. Genc, A. Yilmaz, Y. Yeni, F. Yesilyurt, S. Yildirim, I. Bolat, S. Kordali, F. Yilmaz, A. Hacimuftuoglu, O. Celebi, D. Margina, G.M. Nitulescu, D.A. Spandidos, A. Tsatsakis, Effects of boric acid and potassium metaborate on cytokine levels and redox stress parameters in a wound model infected with methicillin-resistant Staphylococcus aureus, Mol. Med. Rep. 26 (2022), https://doi.org/10.3892/MMR.2022.12809.
[34] M.I. Konaklieva, B.J. Plotkin, Activity of Organoboron Compounds against Biofilm-Forming Pathogens, Antibiotics 13 (2024) 929, https://doi.org/10.3390/ANTIBIOTICS13100929.
[35] V.A. Ponomarev, A.D. Popova, A.N. Sheveyko, E.S. Permyakova, K.A. Kuptsov, A. S. Ilnitskaya, P.V. Slukin, S.G. Ignatov, N.A. Gloushankova, B. Subramanian, D. V. Shtansky, Microstructure and biological properties of titanium dioxide coatings doped with bioactive and bactericidal elements, Appl Surf Sci 575 (2022) 151755, https://doi.org/10.1016/J.APSUSC.2021.151755.
[36] V.A. Ponomarev, A.N. Sheveyko, I.V. Sukhorukova, N.V. Shvindina, A. M. Manakhov, I.Y. Zhitnyak, N.A. Gloushankova, N.K. Fursova, S.G. Ignatov, E. S. Permyakova, J. Polčak, D.V. Shtansky, Microstructure, chemical and biological performance of boron-modified TiCaPCON films, Appl Surf Sci 465 (2019) 486–497, https://doi.org/10.1016/J.APSUSC.2018.09.157.
[37] Z. Sayin, U.S. Ucan, A. Sakmanoglu, Antibacterial and Antibiofilm Effects of Boron on Different Bacteria, Biol Trace Elem Res 173 (2016) 241–246, https://doi.org/10.1007/S12011-016-0637-Z/FIGURES/1.
[38] H. Yang, Y. Wang, X. Xue, Influences of glycerol as an efficient doping agent on crystal structure and antibacterial activity of B-TiO2 nano-materials, Colloids Surf B Biointerfaces 122 (2014) 701–708, https://doi.org/10.1016/J.COLSURFB.2014.08.003.
[39] K.V. Nadaraia, D.V. Mashtalyar, M.A. Piatkova, A.I. Pleshkova, I.M. Imshinetskiy, M.S. Gerasimenko, E.A. Belov, G.A. Zverev, S.L. Sinebryukhov, S.V. Gnedenkov, A first look at the formation of PEO-PDA coatings on 3D titanium, ChemPhysMater 3 (2024) 451–461, https://doi.org/10.1016/J.CHPHMA.2024.07.002.
[40] E.S. Marchenko, G.A. Baigonakova, K.M. Dubovikov, O.V. Kokorev, I.I. Gordienko, E.A. Chudinova, Properties of coatings based on calcium phosphate and their effect on cytocompatibility and bioactivity of titanium nickelide, Materials 16 (2023) 2581, https://doi.org/10.3390/MA16072581.
[41] T. Asada, M. Omichi, T. Kimura, K. Oikawa, Bactericidal effect of calcium oxide and calcined shell calcium on legionella pneumophila, J. Health Sci. 47 (2001) 414–418, https://doi.org/10.1248/JHS.47.414.
[42] İ. Uysal, B. Yılmaz, Z. Evis, Boron doped hydroxapatites in biomedical applications, Journal of Boron 5 (2020) 199–208, https://doi.org/10.30728/BORON.734804.
[43] H. Jodati, A. Tezcaner, A.Z. Alshemary, V. Şahin, Z. Evis, Effects of the doping concentration of boron on physicochemical, mechanical, and biological properties of hydroxyapatite, Ceram Int. 48 (2022) 22743–22758, https://doi.org/10.1016/J.CERAMINT.2022.04.058.
[44] I.V. Fadeeva, K. Barbaro, A. Altigeri, A.A. Forysenkova, M.R. Gafurov, G.V. Mamin, A.V. Knot'ko, V.G. Yankova, A.A. Zhukova, F. Russo, J.V. Rau, Exploring borate-modified calcium phosphate ceramics: antimicrobial potential and cytocompatibility assessment, Nanomaterials 14 (2024) 495, https://doi.org/10.3390/NANO14060495.
[45] K. George, G.-G.-K. Zafiropoulos, Y. Murat, S. Hubertus, R.J. Nisengard, Clinical and microbiological status of osseointegrated implants, J. Periodontol 65 (1994) 766–770, https://doi.org/10.1902/JOP.1994.65.8.766.
[46] S.E. Mountcastle, N. Vyas, V.M. Villapun, S.C. Cox, S. Jabbari, R.L. Sammons, R. M. Shelton, A.D. Walmsley, S.A. Kuehne, Biofilm viability checker: An open-source tool for automated biofilm viability analysis from confocal microscopy images, Npj Biofilms Microbiomes 7 (2021) 1–12, https://doi.org/10.1038/s41522-021-00214-7.
[47] Y.G. Yushkov, A.G. Nikolaev, E.M. Oks, G.Y. Yushkov, investigation of the properties of boron coatings obtained by electron-beam evaporation of pure boron, J. Surf. Invest. 17 (2023) S194–S200, https://doi.org/10.1134/S1027451023070571/FIGURES/6.
[48] Y. Fen Tzeng, S. Ku, S. Chang, C.M. Yang, C.S. Chern, J. Lin, N. Hasuike, H. Harima, T. Ueda, T. Ishigaki, K. Kang, W.S. Yoo, Noncontact, in-line measurement of boron concentration from ultrathin boron-doped epitaxial Si1-xGex layers on Si(100) by multiwavelength micro-Raman spectroscopy, J. Mater. Res. 26 (2011) 739–744, https://doi.org/10.1557/JMR.2010.62/FIGURES/6.
[49] O. Çomaklı, M. Yazıcı, M. Demir, A.F. Yetim, A. Çelik, Effect of bilayer numbers on structural, mechanical, tribological and corrosion properties of TiO2–SiO2 multilayer film-coated β-type Ti45Nb alloys, Ceram Int 49 (2023) 3007–3015, https://doi.org/10.1016/J.CERAMINT.2022.09.285.
[50] N. Laidani, P. Cheyssac, J. Perrière, R. Bartali, G. Gottardi, I. Luciu, V. Micheli, Intrinsic defects and their influence on the chemical and optical properties of TiO2−x films, J. Phys. D Appl. Phys. 43 (2010) 485402, https://doi.org/10.1088/0022-3727/43/48/485402.
[51] M.T. Acar, H. Kovacı, A. Çelik, Comparison of the structural properties, surface wettability and corrosion resistance of TiO2 nanotubes fabricated on Cp-Ti, Ti6Al4V and Ti45Nb, Mater Today Commun 33 (2022) 104396, https://doi.org/10.1016/J.MTCOMM.2022.104396.

[52] V.I. Chukwuike, K. Rajalakshmi, R.C. Barik, Surface and electrochemical corrosion analysis of niobium oxide film formed in various wet media, Appl. Surf. Sci. Adv. 4 (2021) 100079, https://doi.org/10.1016/J.APSADV.2021.100079.
[53] D. Chen, D. Yang, Q. Wang, Z. Jiang, Effects of boron doping on photocatalytic activity and microstructure of titanium dioxide nanoparticles, Ind. Eng. Chem. Res. 45 (2006) 4110–4116, https://doi.org/10.1021/IE0600902/ASSET/IMAGES/LARGE/IE0600902F00009.JPEG.
[54] B.J. Matsoso, K. Ranganathan, B.K. Mutuma, T. Lerotholi, G. Jones, N.J. Coville, Synthesis and characterization of boron carbon oxynitride films with tunable composition using methane, boric acid and ammonia, New J. Chem. 41 (2017) 9497–9504, https://doi.org/10.1039/C7NJ01886J.
[55] G.C. Gomes, F.F. Borghi, R.O. Ospina, E.O. López, F.O. Borges, A. Mello, Nd:YAG (532 nm) pulsed laser deposition produces crystalline hydroxyapatite thin coatings at room temperature, Surf. Coat. Technol. 329 (2017) 174–183, https://doi.org/10.1016/J.SURFCOAT.2017.09.008.
[56] W. Luo, D.Y. Zemlyanov, C.A. Milligan, Y. Du, L. Yang, Y. Wu, P.D. Ye, Surface chemistry of black phosphorus under a controlled oxidative environment, Nanotechnology 27 (2016) 434002, https://doi.org/10.1088/0957-4484/27/43/434002.
[57] M.T. Edmonds, A. Tadich, A. Carvalho, A. Ziletti, K.M. O'Donnell, S.P. Koenig, D. F. Coker, B. Özyilmaz, A.H.C. Neto, M.S. Fuhrer, Creating a stable oxide at the surface of black phosphorus, ACS Appl. Mater. Interfaces 7 (2015) 14557–14562, https://doi.org/10.1021/ACSAMI.5B01297/SUPPL_FILE/AM5B01297_SI_001.PDF.
[58] M. Shimizu, Y. Tsushima, S. Arai, Electrochemical Na-insertion/extraction property of Ni-coated black phosphorus prepared by an electroless deposition method, ACS Omega 2 (2017) 4306–4315, https://doi.org/10.1021/ACSOMEGA.7B00950/ASSET/IMAGES/LARGE/AO-2017-009509_0002.JPEG.
[59] X. Li, C. Dong, Q. Zhao, Y. Pang, F. Cheng, S. Wang, Characterization of Microstructure and Wear Resistance of PEO Coatings Containing Various Microparticles on Ti6Al4V Alloy, J. Mater. Eng. Perform. 27 (2018) 1642–1653, https://doi.org/10.1007/S11665-018-3249-2/FIGURES/11.
[60] X. Zhu, J. Fu, D. Ma, C. Ma, Y. Fu, Z. Zhang, Effect of nano h-BN particles on growth regularity and tribological behavior of PEO composite ceramic coating of ZL109 alloy, Sci. Rep. 12 (2022) 1–12, https://doi.org/10.1038/s41598-022-04768-0.
[61] K. Dong, Y. Song, G. Bian, Y. Cai, E.H. Han, Tribocorrosion behavior of TC18 titanium alloy: A discussion about the interaction between galvanic corrosion and wear, Tribol. Int. 192 (2024) 109292, https://doi.org/10.1016/J.TRIBOINT.2024.109292.
[62] A. Akman, Y. Douest, L.A. Alberta, K. Perrin, A.M. Trunfio Sfarghiu, N. Courtois, B. Ter-Ovanessian, S. Pilz, M. Zimmermann, M. Calin, A. Gebert, Tribocorrosion behaviour of additively manufactured β-type Ti–Nb alloy for implant applications, J. Mater. Res. Technol. 31 (2024) 1419–1429, https://doi.org/10.1016/J.JMRT.2024.06.172.
[63] E. Jiménez-Madrigal, C. Aguilar, L. Béjar-Gómez, E. Cadenas, S. Domínguez-García, M.A. Espinosa-Medina, Corrosion properties of ti-nb-sn alloys prepared by mechanical alloying, J. Mater. Eng. Perform. (2024) 1–17, https://doi.org/10.1007/S11665-024-09651-9/FIGURES/13.
[64] M.T. Acar, H. Kovacı, A. Çelik, Investigation of corrosion and tribocorrosion behavior of boron doped and graphene oxide doped TiO2 nanotubes produced on Cp-Ti, Mater. Today Commun. 32 (2022) 104182, https://doi.org/10.1016/J.MTCOMM.2022.104182.